Design and Experimental Analysis of Novel Multiphase Resonant Motor

Besong John Ebot[1] and Yasutaka Fujimoto[1]

[1]Affiliation not available

June 24, 2024

Design and Experimental Analysis of Novel Multiphase Resonant Motor

Besong John Ebot, *Member, IEEE*, and Yasutaka Fujimoto, *Senior Member, IEEE*

***Abstract*—This paper proposes a novel coreless multiphase magnetic resonant motor (MMRM) with a high torque per unit volume density (77.6 Nm/m^3) based on the properties of magnetic resonance coupling. In the proposed model, the conventional magnetic circuit in electric motors is replaced with that of a resonant circuit. Resonant capacitors are connected across the separate multiphase windings to produce the required resonance behavior in the machine. Analytical models of the machine's characteristics, such as inductance, generated torque, and capacitance estimation are derived and verified with an equivalent simulation model through finite element methods. The key is to efficiently integrate electric machine design concepts with inductive magnetic resonance coupling technology to enhance the output torque in an air-cored machine. The motor consists of a two-phase multiphase stator and rotor windings arranged radially on non-magnetic cores made from reinforced plastic fiber. Finally, a prototype is manufactured, and the effectiveness of the MMRM is validated by experimental results. To evaluate the significance of the proposed design, a case-control experiment without resonant capacitors is set up. The proposed MMRM achieved improved performance compared to related resonant induction machines.**

***Index Terms*—multiphase resonant motor, multi-phase coils, wireless resonant power transfer, resonant circuit, air-cored machine, non-magnetic cores.**

I. Introduction

ELECTRIC machines play an essential part to our lives, creating global environmental concerns about sustainability. Historically, electric machines are made from two main materials: silicon steel cores, used as a suitable conduit for magnetic flux and copper or aluminum used as current conductors [1]. For improved performance, permanent magnet (PM) types are widely used. However, the price of magnets highly influences the cost of electric machines. Reducing manufacturing complexity, and thus cost is a key issue in machine design today [2].

Recently, the magnetic resonance coupling first reported in [3] and extensively studied in [4]−[7], is presenting new sustainable alternative approaches to electric machine design. In these approaches, the PM and percentage of the magnetic steel cores utilized is reduced or completely removed [8]−[12]. The electric machine models designed following these approaches are coreless with no ferromagnetic material for field conduits and no hysteresis losses. In essence, the conventional magnetic circuit present through the ferromagnetic cores is replaced with a proposed resonant magnetic circuit [13]−[18].

Magnetic resonance coupling through a proposed resonant circuit compensate for the removed magnetic flux density conduit. Consequently, the machin's efficiency varies with

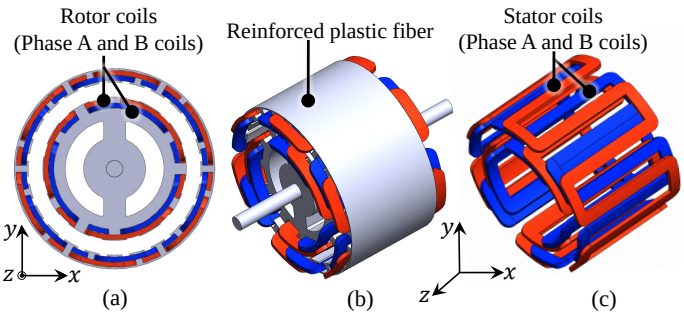

Fig. 1. A 3-D CAD model of a multi-phase magnetic resonant motor. The different phase coils are shown in red and blue.

resonant frequency as reported by [8]−[9], [19]−[21]. This paper proposes a coreless multiphase magnetic resonant motor (MMRM) that adopts the approach of replacing the ferromagnetic iron stator and rotor cores with a reinforced plastic fiber material. The MMRM is an air-cored resonant multiphase induction machine with improved torque density enhanced through magnetic resonance coupling. The MMRM model exploits the benefits of reduced torque ripple and increase fault tolerance usually found in multiphase induction machines [22].

The 3-D conceptual model of the MMRM is shown in Fig. 1. The multiphase windings in the MMRM has a symmetrical structure wound around a non-magnetic reinforced plastic fiber cores (cf. Fig. 1(a) and 1(b)). Since the motor has no magnetic core, the air-gap in the machine is simply measured as the length separating stator and rotor multiphase windings. In order to enhance the power rating performance, capacitors of the resonant circuit are connected in series to the phase windings. This offsets the inductive reactance of the motor, achieves resonance at a set slip and improves the electrical load for specific voltages. The compensation of the leakage inductance voltage drop through resonance capacitance increases the current within a constant rated voltage [7]. As the effective motor impedance reduces, the torque performance increases. The non-magnetic core structure of the machine eliminates self-excitation with the series capacitors usually a drawback in induction machines, and significantly reduces the machine's magnetic loading.

Similar high-speed air-cored resonant induction machines are reported by [10]− [19] in which circuits models are equivalent. However, the topological structure in [15]−[17] is a 3-phase machine different from the 2-phase machine structure described in [8]−[9]. Furthermore, the reported characteristics of the machine are solely derived from FEA analysis, without an accompanying established analytical model. In [8], a linear-type MMRM is described and in [12]− [13] the model is extended to a radial-gap type with analytical verification for

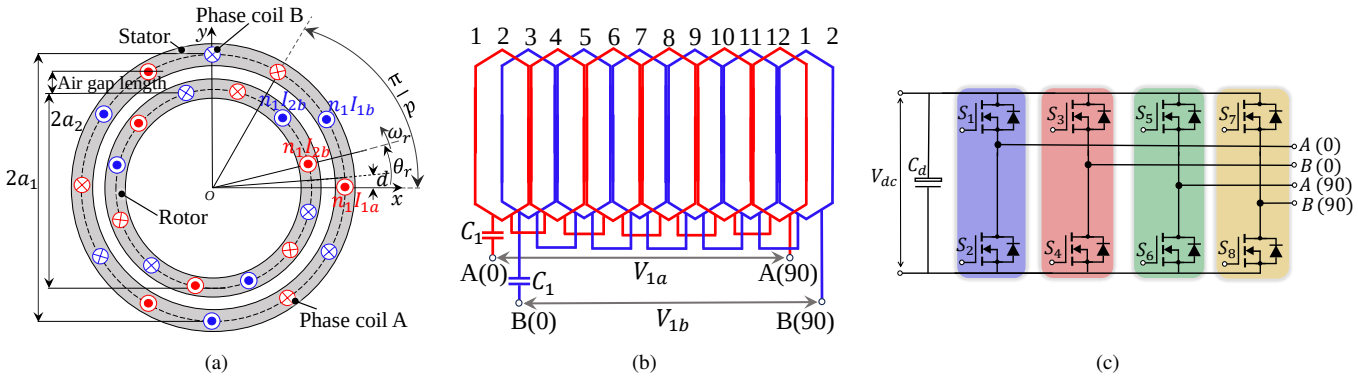

(a) (b) (c)

Fig. 2. Topology of the proposed MMRM. (a) The basic conceptual model. (b) Stator field winding connected relation and the multi-phase inverter connecting points. (c) Proposed 4-ϕ multi-phase high frequency inverter topology and stator phase windings connected points. The pole pitch defined from an air-gap diameter of $2a_2$ is expressed as $\tau_p = 2\pi a_2/p$, and the electric angle $\theta = (\pi/\tau_p)\theta_r$. θ_r is the rotor mechanical angle.

different air gap lengths. In [12], numerical models and operational conditions are presented. In [17], an alternative approach is employed, leveraging the concept of frequency splitting to generate an excitation sequence in a multi-phase stator phase winding system. The torque computed via FEA is minimal, and the paper does not include any theoretical model of the motor parameters. In [14], 3-D analytical method for computed inductance in resonant induction machines is reported but requires high computational power. The proposed MMRM offers practical advantages such as eliminating saturation and iron losses, possessing good overload capability, low inertia and cogging torque, achieving high efficiency during high-speed operation, and being straightforward to implement [8]–[18]. Beyond the utilization of magnetic resonance coupling and its characteristics in a consolidated approach to design an electromechanical energy conversion system, the main contributions in this paper are as follows.

1) A simplified analytical model of the MMRM to compute the inductance, torque etc.
2) The design and construction of an experimental prototype of the MMRM based on magnetic resonance coupling, with its associated implemented inverter to operate it.

The rest of the article is arranged as follows. In Section II, the topology, operational principles and basic analytical modeling of the MMRM are discussed. Section III presents FEA analysis. Section IV discusses the experiments and results. In Section V a comparative analysis with related resonant machines is shown and Section VI concludes the article.

II. Topology and Operational Principle of The MMRM

A. The Machine Topology and Operation Principle

A conceptualized 2-D equivalent section model of the MMRM illustrating the coils configuration and the direction of current flow is shown in Fig. 2(a). Four separate windings are used in the motor, two in the stator and two in the rotor. Each phase winding is isolated from the other and connected to separate equivalent capacitances. The stator winding diagram indicating connection points of the stator field winding is depicted in Fig. 2(b). The phase windings are tied to a high frequency multiphase inverter following the connection points A(0)−A(90) and B(0)−B(90) as shown in Fig. 2(c). The inverter injects a two phase power supply, with 90-degree phase difference. Having capacitors in each phase of the multiphase winding, connected to a multiphase inverter, offers the benefit of minimizing winding harmonics. The operation of the MMRM is similar to that of conventional induction motors [22], but in MMRM, current is induced in the rotor side through magnetic resonance coupling technology. Resonance is achieved by adding capacitance to all the phase windings of the motor to formed an LC coupled system.

To create the rotary actuation mechanism in MMRM, a rotating magnetic field flux is set up through two sinusoidal voltage sources with 90-degree phase difference. The voltage sources driven by the high frequency inverter are connected to fixed multiphase stator windings through equivalent capacitances (C_{1a}, C_{1b}) and $C_{1a} = C_{1b} = C_1$. The rotating fields induces currents through magnetic resonance coupling in the closed loops multiphase rotor winding. The multiphase rotor windings form a closed loops with equivalent capacitances (C_{2a}, C_{2b}) and $C_{2a} = C_{2b} = C_2$ connected to them. The induced currents in the rotor multiphase coils set up magnetic field around it. This causes it to follow the main fields as it rotates. The voltage source frequency is nearly equal to the system's resonant frequency.

B. Inductance Modeling

The generated magnetic field is modeled using Ampere's law considering the number of turns n carrying current I as

$$\boldsymbol{H}_0(x,y) = \begin{bmatrix} H_{0x}(x,y) \\ H_{0y}(x,y) \end{bmatrix} = \frac{nI}{2\pi(x^2+y^2)} \begin{bmatrix} -y \\ x \end{bmatrix} \quad (1)$$

where $\boldsymbol{H}_0(x,y)$ is the magnetic field vector at position (x,y). According to Fig. 2(a), the total magnetic field generated by the stator windings at the circumferential points of the stator core is described as [13]

$$\boldsymbol{H}_1(x,y) = \sum_{k=0}^{2p-1} (-1)^k \boldsymbol{H}_0(x - a_1 \cos\frac{2\pi k}{p}, y - a_1 \sin\frac{2\pi k}{p}) \quad (2)$$

where p represents the number of pole pairs, k is the winding constant accounting for the coil pitch and distribution factors,

a_1 and a_2 denote the radii from the origin O to the stator and rotor windings respectively. The winding phase inductance derived from the self-flux linkage is written in the form [13]

$$L_i = L_{ex} + L_{in}. \tag{3}$$

L_{ex} represents the portion of the inductance related to the fields outside to the coil winding confined within $[d/a_1, \pi/p - d/a_1]$, while L_{in} corresponds to the portion related to the energy of the fields inside the wire within the windings, bounded by $[0, d/a_1]$. The generalized form of L_i is written as

$$L_i = \underbrace{-\frac{\mu_0 l_z n_1^2}{\pi} \log\left[\tan\left(\frac{pd}{2a_1}\right)\right]}_{:=L_{ex}} - \underbrace{\frac{\mu_0 l_z n_1^2}{\pi}\left(\frac{qa_1}{d}\right)\int_0^{\frac{d}{a_1}} \sum_{k=0}^{2p-1} \frac{(-1)^k}{2\tan(\frac{k\pi}{2p} - \frac{q}{2})} dq}_{:=L_{in}}. \tag{4}$$

The variable q is a spatial angle and l_z is the stack length. The phase inductance confined in the stator and the rotor windings can be calculated using (4). when dealing with very small wire sizes, it is assumed that the current density is uniformly spread across the wire, and L_{in} is omitted from the model.

The mutual flux linkage between the stator and rotor windings derived along with the angular position of the rotor is expressed as

$$\Phi_{12} = -\frac{\mu_0 l_z n_1 n_2 I_1}{2\pi} \log \frac{a_r^{2p} - 2a_r^p \cos(p\theta) + 1}{a_r^{2p} + 2a_r^p \cos(p\theta) + 1}. \tag{5}$$

From (5), the corresponding mutual inductance is written as

$$M(\theta) = \frac{\Phi_{12}}{I_1} = -\frac{\mu_0 l_z n_1 n_2}{2\pi} \log \frac{a_r^{2p} - 2a_r^p \cos(p\theta) + 1}{a_r^{2p} + 2a_r^p \cos(p\theta) + 1}. \tag{6}$$

Additional computation yields an approximation of (6) as

$$M(\theta) \approx M_1 \cos(p\theta) + M_3 \cos(3p\theta) \tag{7}$$

$$M_1 = \frac{p}{\pi}\int_0^{\frac{2\pi}{p}} M(\theta)\cos(p\theta)d\theta = \begin{cases} \dfrac{2\mu_0 l_z n_1 n_2}{\pi a_r^p} & (a_r > 1) \\ \dfrac{2\mu_0 l_z n_1 n_2}{\pi a_r^{-p}} & (a_r < 1) \end{cases} \tag{8}$$

$$M_3 = \frac{p}{\pi}\int_0^{\frac{2\pi}{p}} M(\theta)\cos(3p\theta)d\theta = \begin{cases} \dfrac{2\mu_0 l_z n_1 n_2}{3\pi a_r^{3p}} & (a_r > 1) \\ \dfrac{2\mu_0 l_z n_1 n_2}{3\pi a_r^{-3p}} & (a_r < 1) \end{cases} \tag{9}$$

$$M(\theta) \approx \begin{cases} \dfrac{2\mu_0 l_z n_1 n_2}{\pi a_r^p}(\cos(p\theta) + \dfrac{1}{3a_r^{2p}}\cos(3p\theta)) & (a_r > 1) \\ \dfrac{2\mu_0 l_z n_1 n_2}{\pi a_r^{-p}}(\cos(p\theta) + \dfrac{1}{3a_r^{-2p}}\cos(3p\theta)) & (a_r < 1) \end{cases} \tag{10}$$

where $a_r = a_1/a_2$ and θ is the rotor electrical angle. In this article, $a_1/a_2 > 1$. Changes in the mutual inductance $M(\theta)$ with θ due to the generated torque is given by (10).

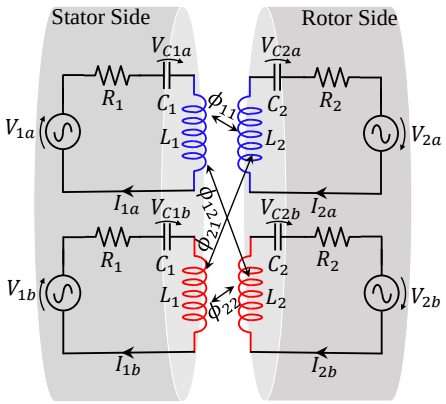

Fig. 3. Equivalent electric circuit model of the MMRM.

C. Machine Circuit Analysis

A key design step is choosing the suitable resonant topology for the MMRM that can achieves high currents in the rotor. The SS resonance compensation method is applied in the machine to minimizes the stator winding impedance and maximizes current in rotor side [10], [23]– [24]. The SS compensation also achieves strong response to changes in coupling coefficients and good for applying high currents at low voltages with high speeds.

The equivalent electric circuit model of the MMRM is shown in Fig. 3. The resonant interaction between the stator and rotor windings alters as the rotor rotates. The inductance matrix $\boldsymbol{L}$ is written as

$$\boldsymbol{L} = \begin{bmatrix} L_1 & 0 & M_0\cos\theta & -M_0\sin\theta \\ 0 & L_1 & M_0\sin\theta & M_0\cos\theta \\ M_0\cos\theta & M_0\sin\theta & L_2 & 0 \\ -M_0\sin\theta & M_0\cos\theta & 0 & L_2 \end{bmatrix} \tag{11}$$

where M_0 is the optimum value of the mutual inductance between multiphase windings. The stator and rotor coil inductance are L_1 and L_2 respectively, obtained from (4). The voltage equation is written as

$$\boldsymbol{V} = \boldsymbol{RI} + \frac{d}{dt}(\boldsymbol{LI}) + \boldsymbol{V}_C \tag{12}$$

$$\boldsymbol{I}_C = \boldsymbol{C}\frac{d\boldsymbol{V}_C}{dt} \tag{13}$$

where

$$\boldsymbol{V} = [V_{1a} \quad V_{1b} \quad V_{2a} \quad V_{2b}]^{\mathrm{T}} \tag{14}$$

$$\boldsymbol{I} = [I_{1a} \quad I_{1b} \quad I_{2a} \quad I_{2b}]^{\mathrm{T}} \tag{15}$$

$$\boldsymbol{R} = \mathrm{diag}(R_1, \quad R_1, \quad R_2, \quad R_2) \tag{16}$$

$$\boldsymbol{C} = \mathrm{diag}(C_1, \quad C_1, \quad C_2, \quad C_2) \tag{17}$$

$$\boldsymbol{V}_C = [V_{C1a} \quad V_{C1b} \quad V_{C2a} \quad V_{C2b}]^{\mathrm{T}} \tag{18}$$

and V_{1a}, V_{1b}, V_{2a}, and V_{1b} are the windings terminal voltages. I_{1a}, I_{1b}, I_{2a} and I_{2b} are currents in each phase winding. R_1 and R_2 are winding resistances, C_1 and C_2 are resonance capacitors connected to the phase windings and V_{C1a}, V_{C1b}, V_{C2a} and V_{C2b} the corresponding capacitor voltages.

D. Torque Generation

Considering that the currents flowing through the multi-phase windings are expressed in the form

$$I_{1a} = I_1 \sin(\omega_1 t) \tag{19}$$

$$I_{1b} = I_1 \sin(\omega_1 t - \frac{\pi}{2}) \tag{20}$$

$$I_{2a} = I_2 \sin(\omega_2 t - \delta) \tag{21}$$

$$I_{2b} = I_2 \sin(\omega_2 t - \delta - \frac{\pi}{2}) \tag{22}$$

where δ is the phase delay between the current in the stator and rotor windings. I_1 and ω_1 denote the amplitude and the angular frequency of the current in the stator winding, while I_2 and ω_2 corresponds to that in the rotor side. The terminal voltage V_{1a}, V_{1b}, V_{2a}, and V_{2b} is expressed as

$$\begin{aligned} V_{1a} = {} & R_1 I_1 \sin(\omega_1 t) + (\omega_1 L_1 - \frac{1}{\omega_1 C_1}) I_1 \cos(\omega_1 t) \\ & + (\omega_2 + \omega) M_0 I_2 \cos(\omega_2 t + \theta - \delta) \end{aligned} \tag{23}$$

$$\begin{aligned} V_{1b} = {} & -R_1 I_1 \cos(\omega_1 t) + (\omega_1 L_1 - \frac{1}{\omega_1 C_1}) I_1 \sin(\omega_1 t) \\ & + (\omega_2 + \omega) M_0 I_2 \sin(\omega_2 t + \theta - \delta) \end{aligned} \tag{24}$$

$$\begin{aligned} V_{2a} = {} & R_2 I_2 \sin(\omega_2 t - \delta) + (\omega_2 L_2 - \frac{1}{\omega_2 C_2}) I_2 \cos(\omega_2 t - \delta) \\ & + (\omega_1 - \omega) M_0 I_1 \cos(\omega_1 t - \theta) \end{aligned} \tag{25}$$

$$\begin{aligned} V_{2b} = {} & -R_2 I_2 \cos(\omega_2 t - \delta) + (\omega_2 L_2 - \frac{1}{\omega_2 C_2}) I_2 \sin(\omega_1 t - \delta) \\ & + (\omega_1 - \omega) M_0 I_1 \sin(\omega_1 t - \theta). \end{aligned} \tag{26}$$

The theoretical torque generated can be written [13]

$$\begin{aligned} T_e &= \frac{\partial W}{\partial \theta_r} = \frac{d\theta}{d\theta_r} \frac{1}{2} \boldsymbol{I}^T \frac{\partial \boldsymbol{L}}{\partial \theta} \boldsymbol{I} \\ &= \frac{\pi}{\tau_p} I_1 I_2 M_0 \sin((\omega_1 - \omega_2)t - \theta + \delta). \end{aligned} \tag{27}$$

Each rotor sub-phase winding is short circuited with external capacitors connected through it. The requirement for the rotor winding terminal voltages V_{2a} and V_{2b} to meet $V_{2a} = V_{2b} = 0$ is given by

$$\delta = -\tan^{-1} \frac{R_1}{\omega_2 L_2 - \frac{1}{\omega_2 C_2}} \tag{28}$$

$$I_2 = -\frac{\omega_2 M_0}{\sqrt{R_2^2 + (\omega_2 L_2 - \frac{1}{\omega_2 C_2})^2}} I_1 \tag{29}$$

$$\omega_2 t = \omega_1 t - \theta \tag{30}$$

$$\omega_2 = \omega_1 - \omega. \tag{31}$$

When the torque in the MMRM is controlled by a voltage source V_1, and $V_1 = \sqrt{V_{1a}^2 + V_{1b}^2}$ such that

$$V_{1a} = I_1 A \cos(\omega_1 + \beta) \tag{32}$$

$$V_{1b} = I_1 A \sin(\omega_1 + \beta) \tag{33}$$

where

$$A = \sqrt{R_1^2 + X_1^2 + \frac{\omega_1 \omega_2 M_0^2 (\omega_1 \omega_2 M_0^2 + R_1 R_2 - X_1 X_2)}{R_2^2 + X_2^2}} \tag{34}$$

$$\beta = \tan^{-1} \frac{\omega_1 \omega_2 M_0^2 R_2 + R_1 (R_2^2 + X_2^2)}{\omega_1 \omega_2 M_0^2 X_2 - X_1 (R_2^2 + X_2^2)} \tag{35}$$

$$X_1 = \omega_1 L_1 - \frac{1}{\omega_1 C_1} \tag{36}$$

$$X_2 = \omega_2 L_2 - \frac{1}{\omega_2 C_2}. \tag{37}$$

The generated has the rewritten as

$$T_{e,v} = \frac{\pi}{\tau_p} \frac{(\omega_1 - \omega) M_0^2 R_2}{D} V_1^2 \tag{38}$$

where

$$\begin{aligned} D = {} & (R_1^2 + X_1^2)(R_2^2 + X_2^2) \\ & + \omega_1 \omega_2 M_0^2 (\omega_1 \omega_2 M_0^2 + 2 R_1 R_2 - X_1 X_2). \end{aligned} \tag{39}$$

III. Numerical Analysis

A. FEM Analysis

The magnetic field frequency analysis of the equivalent 3-D CAD model of the MMRM is analyzed by finite element method (FEM). The analytical model of all integral quantities (L_i, M_0 and T_e) is validated through the 3-D FEM analysis. The MMRM model topology used in the analysis is a two phase, six pole-pair machine. The 3-D FEM-computational models improves the accuracy of the winding inductance if comapred to 2-D FEM models discussed in [9]. All FEM analysis were conducted using *JMAG-Designer-ver-19*. The MMRM and its corresponding circuit analysis model is shown in Figs. 4 and 5 respectively. The design parameters is shown in Table I.

B. Resonance Frequencies

The capacitance values are computed to compensate for the equivalent MMRM phase inductances at the resonance frequency of the MMRM. The frequency model utilize for the computation of the required capacitance is described in [13] as follows.

$$\omega_{res} = \left\{ \frac{1}{\sqrt{(\sqrt{L_1 L_2} - M_0) \sqrt{C_1 C_2}}} + \frac{\omega}{2}, \; \frac{1}{\sqrt{(\sqrt{L_1 L_2} + M_0) \sqrt{C_1 C_2}}} + \frac{\omega}{2} \right\}. \tag{40}$$

It is important to note the existence of a winding capacitance in the phase coils of the machine. In the MMRM presented in this paper, it is in order of $\frac{1}{1000}$ μF. As a result, the compensating capacitance is totally dependent on the added capacitors.

IV. Experimental Validation and Analysis

In this section, comprehensive experimental results of the proposed MMRM are presented. We begin with discussions on critical issues of the experimental setup configuration, then proceeds with how the experiments are conducted and results extracted.

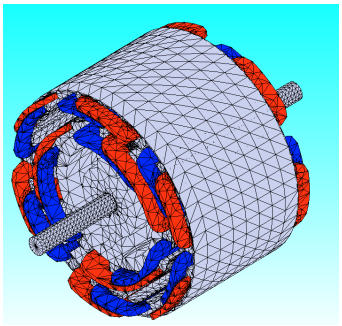

Fig. 4. Model for magnetic field analysis by FEM.

TABLE I
SPECIFICATION OF THE MAGNETIC RESONANT MOTOR PROTOTYPE

Parameters	Stator	Rotor
Outer diameter [mm]	a_1 = 94	a_2 = 74
Equivalent capacitance [μF]	C_1 = 270	C_2 = 330
Winding resistance [mΩ]	324	254
Number of turns (turn/phase)	400	320
Stack length l [mm]	85	
Mechanical gap length Ag [mm]	12	
Resonance frequency f_0 [kHz]	1	
Litz wire	2UEWLZ 40×0.2 mm	
Stator resonant caps.	947D271K112AEGSN	
Rotor resonant caps.	KTD500B227M99A0B00	

A. Experimental Setup

To validate the FEM-computed model of the proposed MMRM, an experimental prototype was developed and tested. The experimental test bench for the developed prototype is shown in Fig. 6(a). To evaluate and determine the significance of the proposed MMRM, a case-control experiment was conducted without resonant capacitors. To achieve this, two rotors were implemented. One with resonant capacitors integrated into the reinforced plastic rotor core (MMRM) and the other without capacitors known as a pure coreless inductive multiphase motor (PCIMM). This is shown in Fig. 6(b). The specifications of the implemented MMRM, resonant capacitors and Litz wire are all shown in Table I. The selected capacitors can withstand high currents and cancel out the terminal reactance at resonance frequency f_0. The details of the rotor winding with capacitors placement is shown in Fig. 6(c). A similar layout is implemented in the stator side. An originally developed four-phase (4-ϕ) high frequency inverter with eight GaN-HEMT based on the circuit topology illustrated in Fig. 5 is used to drive the prototype MMRM. The GaN-HEMT are connected as four half bridge modules all connected to a control board as shown in Fig. 6(a). The control board is made of a single digital signal processor (DSP) of type TMDSCNCD28379D based on the TMS320F28069. The DSP is used as the main controller to generate gate signals and manage the interaction of the half-bridge modules. The switching frequency was set to f_{sw} = 100 kHz.

A rotary speed encoder attached to the rotating shaft, type MTL MEH-30-300PE-P detects the speed by generating 3000

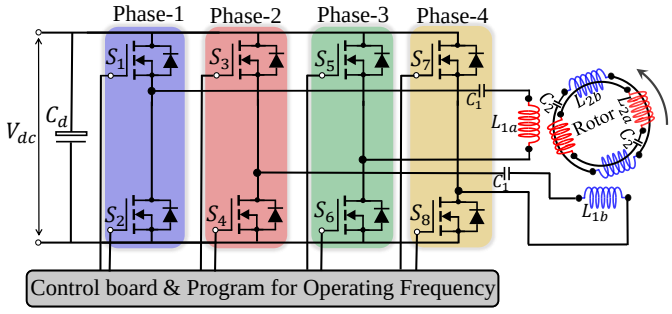

Fig. 5. The topology of the implemented experimental resonant motor. The stator windings are connected to the proposed 4-ϕ inverter. The circuit layout model is utilized for FEM-computed FEA analysis.

pulses per revolution. The UNIPULSE UTMII−2Nm torque sensor measures the drive torque. The K-type thermocouple wires are attached to each stator phase winding to track the temperature as the machine operates. A hysteresis brake, type MAGTROL HB-250-M2 attached on the load side of the torque meter through the rotating shaft, serves as the load. The maximum applicable load torque in the experiment is generated applying a maximum current of 0.02 A to the brake. The MyWay PE-Expert4 digital control system captures all signals from torque sensor, rotary encoder and thermocouple wires. A data processing program was implemented in a DSP control board of the MyWay PE-Expert4 to determine the drive torque, speed and temperature in the stator phase windings. All data were processed with the PE-ViewX software installed in the PC. The complete setup for the experimental verification is shown in Fig. 6(d).

B. Experimental Results

The FEM-computed and measured phase inductances of the MMRM are shown in Table II. It can be observed that FEM-computed values deviates 4.2% to 5.5% from measured inductance values. All phase inductances were measured at 1 kHz using the NF-ZM2372 LCR meter.

The resonance frequency applied in MMRM is f_0 = 1 kHz. The waveform of the measured current in the stator phase windings I_{1a} and I_{1b} in both MMRM and PCIMM is shown in Fig. 7(a) and 7(b) respectively. In the PCIMM a peak-to-peak current of 20.95 A is utilized compared to running in it as an MMRM that uses 12.54 A peak-to-peak.

To determine the steady state and transient torque limits of the MMRM, torque responses from f_0 = 0.1 kHz to f_0 = 2 kHz is obtained analytically, by FEA and through experiments as shown in Fig. 8(a). In all cases, the torque response are maximum around f_0 = 1 kHz. Experimentally, 0.183 Nm torque was achieved while those obtained analytically and by simulation were 0.149 Nm and 0.140 Nm respectively. As a results of frequency splitting, a second domain of torque response up to 0.09 Nm is generated for the analytical case around f_0 = 1.5 kHz. In experiment, it reached 0.08 Nm. The supply voltage increases with increase in supply frequency due to increasing terminal impedance. The transient torque achieved experimentally operating the motor in PCIMM and MMRM modes are shown in Fig. 8(b) and 8(c) respectively.

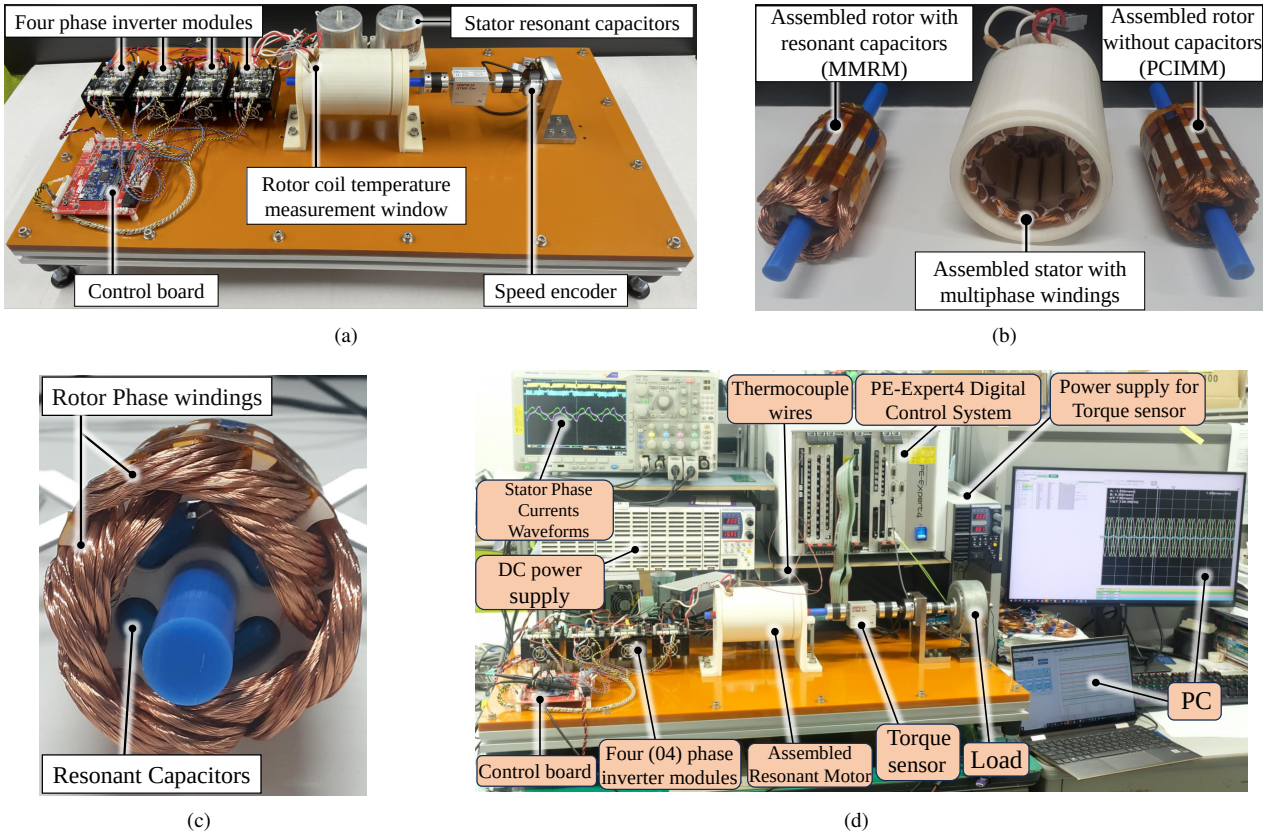

Fig. 6. Photographs of the implemented prototype. (a) Experimental test bench (b) Assembled stator and rotors of the MMRM. (c) The multiphase rotor coils showing capacitor placement integrated into the rotor core. (d) Complete experimental setup for testing the MMRM.

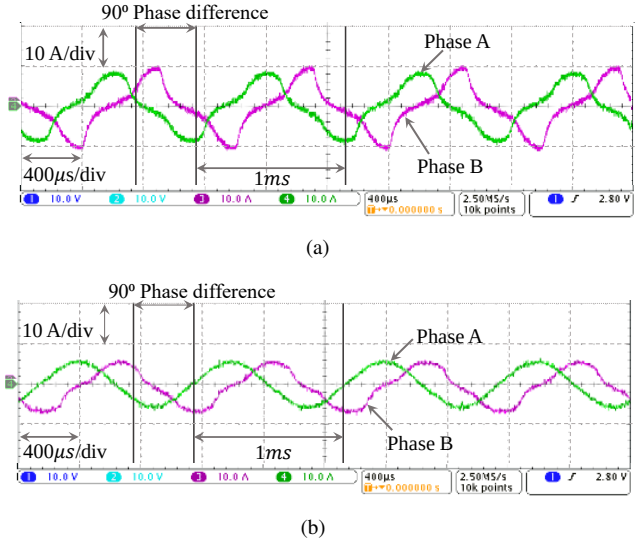

Fig. 7. Waveforms of measured stator phase windings currents, I_{1a} (Phase A) and I_{1b} (Phase B). (a) Current during operation as PCIMM. (b) Current during the operation as a MMRM.

As shown in Fig. 8(d), the maximum torque reached in PCIMM mode is 0.048 Nm while in the MMRM it is 0.183 Nm. In the PCIMM, the maximum speed recorded was 186 min^{-1} while in MMRM 596 min^{-1} was recorded as shown in Fig 8(e). The torque produced in the PCIMM is very sensitive to the load.

TABLE II
MEASURED AND FEM-COMPUTED EQUIVALENT CIRCUIT PARAMETERS

Parameter	Variable	Measured	Calculated	Error
Stator phase A	L_{1a}	96.40 μH	91.78 μH	5.0%
Stator Phase B	L_{1b}	95.23 μH	91.40 μH	4.2%
Rotor Phase A	L_{2a}	76.24 μH	72.27 μH	5.5%
Rotor Phase B	L_{2b}	76.32 μH	72.38 μH	5.4%

Temperature fluctuations within the stator windings are maintained within an acceptable range for Litz wire, even with an increase in current during the experiment. In the MMRM, temperature of up to 71 °C was measured after about 300 seconds operating the machine with load torque of 0.0183 Nm, while the temperature reached 92 °C with load torque of 0.048 Nm in the PCIMM. This is shown in Fig. 8(f). The temperature of the rotor coils are measured through a temperature measurement window found on the front cover of the motor. The measurements are taken using the FLUKE Ti100 thermal imager are shown in Fig. 9. As shown in the figures, the temperature is lower when the machine is operated as MMRM.

C. Loss and Efficiency

A merit of the MMRM is that it has no ferromagnetic iron core to characterizes sources of loss as in conventional motors. Losses in the MMRM is mainly copper losses (P_{cu})

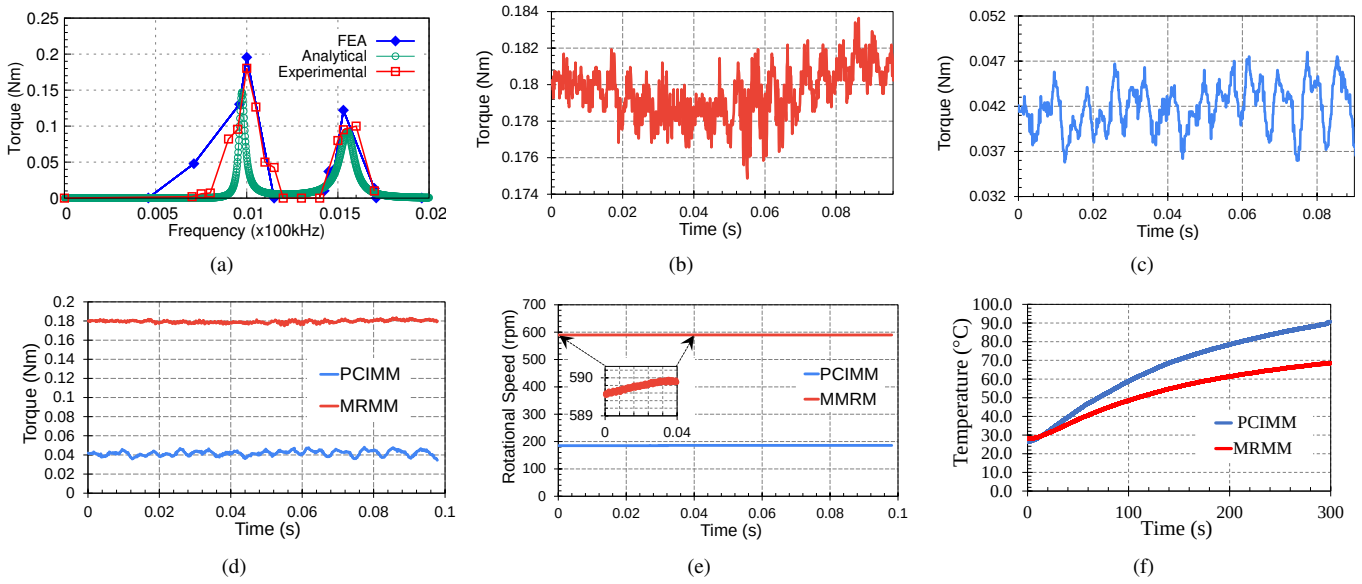

Fig. 8. Experimental results of the MMRM. (a) Torque (Nm) performance for FEA, analytical and experimental model of the MMRM. (b) Experimental transient toque performance at resonance f_0 = 1 kHz. (c) Torque performance for the PCIMM. (d) Comparing the MMRM and PCIMM performance. (e) Speed (rpm) performance in the MMRM and PCIMM. (f) Temperature (℃) changes in the MMRM and PCIMM after operating within 5 minutes.

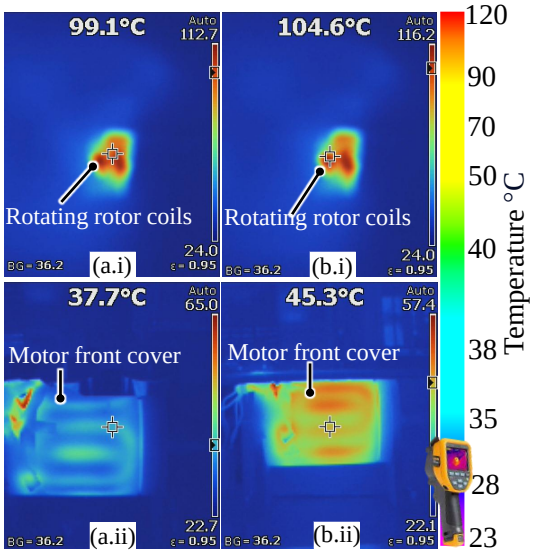

Fig. 9. Thermal imager temperature recordings. (a.i) Temperature measurement of MMRM rotor phase coils. (a.ii) MMRM front cover. (b.i) Temperature measurement of PCIMM rotor phase coils. (b.ii) PCIMM front cover.

due to measured phase currents and corresponding windings resistances (R_n) expressed as

$$P_{cu} = \left(\sum_{n=1}^{6} R_n I_{rms,n}^2 \right). \tag{41}$$

In the experiment, $I_{1a} = I_{1b} = 12.54$ A and the loss in the stator $P_{cu} = 50.95$ W. The change in temperatures observed during the experiment characterize the losses. The efficiency of the MMRM is written the form

$$\eta = \frac{P_{out}}{P_{out} + P_{cu}} \tag{42}$$

where P_{out} is defined as $P_{out} = T_e \times \omega_r$. At speed $\omega_r = 596$ min^{-1}, the efficiency of the MMRM is estimated as 38.17%.

V. Discussions

A robust study that qualitatively and quantitatively compared the proposed MMRM with other related resonant machines has been conducted and is shown in Table III. Of these [11]− [19], the MMRM has the largest air-gap length and highest torque per unit volume of 12 mm and 77.56 Nm/m^3 respectively. It also achieved the highest efficiency (38.17%) of all currently implemented resonant induction machines with record measured experimental speed of 589 min^{-1}.

Quality factor Q is a good figure of merit to evaluate the performance of the MMRM. It limits power transfer efficiency between the stator and rotor phase coils [23]−[24]. At 1 kHz, the Q−factor in the stator and rotor coil of the MMRM is Q_1 = 1.8684 and Q_2 = 1.8850 respectively. This is quite small but is justified by the small size of the implemented machine. This limits the winding inductance.

VI. Conclusion

In this article, a model design, analysis and experimental verification of the novel multiphase coreless magnetic resonant motor is presented. The developed prototype is is a six-pole machine with additional capacitances connected across its multiphase windings. To evaluate the significance and performance of the motor, an equivalent non-resonant model was developed as case-control experiment. The developed machine has a high torque per unit volume density of 77.56 Nm/m^3, higher compared to all related resonant induction machines.

The proposed motor is expected to be used in lightweight applications where weight and size are critical, such as in micro-robots where extremely small bodies require actuation. To the best of the authors' knowledge, the machine presented in this article represents the first experimental validation of a two-phase magnetic resonant motor.

TABLE III
COMPARISON OF THE MMRM TO OTHER IMPLEMENTED RESONANT INDUCTION MACHINES

	Proposed MMRM	MRC Motor	ACRIM	MRCM-2	SCMR	UAMRM
Reference paper	—	[11]	[15]	[17]	[18]	[19]
Analytically evaluated	✓	×	✓	✓	✓	×
Experimentally evaluated	✓	✓	✓	×	✓	✓
Number of phases/pole-pair	2/6	3/8	3/8	5/10	1/4	2/4
Mechanical length of airgap [mm]	12	1	1	1	10	3
Effective length [mm]	120	150	—	200	80	—
Outer diameter [mm]	94	206	—	150	80	200
Maximum speed [min^{-1}]	589	60	—	1000⋆	—	—
Maximum torque [Nm]	0.183	0.164	1.023	1.0678⋆	0.003	0.142
Torque per unit volume [Nm/m^3]	77.56	8.20	—	77.53	1.87	1.87
Efficiency	38.17%	9.57%	28.20%	36.61%⋆	—	—

Abbreviation: ⋆ indicates values obtained through simulation
SCMR: strongly coupled magnetic resonance system
MRCM: magnetic resonance coupling motor
ACRIM: air-cored resonant induction machines
UAMRM: Ultra-lightweight axial magnetic resonant motor

REFERENCES

[1] C. Liu, "Emerging electric machines and drives – An overview," *IEEE Trans. Energy Convers.,* vol. 33, , no. 4, pp. 2270−2280, Dec. 2018.

[2] K. T. Chau, C. C. Chan and C. Liu, "Overview of permanent-magnet brusless drives for electric and hybrid electric vehicles," *IEEE Trans. Ind. Electron.,* vol. 55, no. 6, pp. 2246−2257, June. 2008.

[3] A. Kurs, A. Karalis, R. Moffatt, J.D. Joanopoulous, P. Fisher and M. Soljacic , "Wireless power transfer via strongly coupled magnetic resonance," *Science,* vol. 317, no. 5838, pp. 83−86, Jul. 2007.

[4] Z. Zhang, H. Pang, A. Georgiadis and C. Cecati, "Wireless power transfer − An overview," *IEEE Trans. Ind. Electron.,* vol. 66, no. 2, pp. 1044−1058, Feb. 2019.

[5] M. Liu, H. Zhang, Y. Shao, J. Song and C. Ma, "High-performance megahertz wireless power transfer: Topologies, modeling, and design," *IEEE Ind. Electron. Mag.,* vol. 15, no. 1, pp. 28−42, Mar. 2021.

[6] M. Fu, Z. Tang and C. Ma, "A critical review of recent progress in mid-range wireless power transfer," *IEEE Trans. Power Electron.,* vol. 29, no. 9, pp. 4500−4511, Sept. 2014.

[7] A. P. Sample, D. T. Meyer and J. R. Smith, "Analysis, experimental results, and range adaptation of magnetically coupled resonators for wireless power transfer," *IEEE Trans. Ind. Electron.,* vol. 58, no. 2, pp. 544−554, Feb. 2011.

[8] Y. Fujimoto, "Modeling and analysis of wireless electro-mechanical energy transfer and conversion using resonant inductive coupling," in *Proc. 41st Annu. Conf. IEEE Ind. Electron. Soc.,* Nov. 2015, pp. 4905−4910.

[9] J. E. Besong and Y. Fujimoto, "Design of a coreless multi-phase electric motor using magnetic resonant coupling," in *IEEE Trans. Magn.,* vol. 58, no. 9, pp. 1−11, Sept. 2022, Art no. 8206611, doi:10.1109/TMAG.2022.3193055.

[10] Boyvat, M., Hafner, C. and Leuthold, J., "Wireless control and selection of forces and torques − towards wireless engines," *Sci Rep 4*, no. 5681, 2014.

[11] K. Takishima, and K. Sakai, "Design method for ultralightweight motor using magnetic resonance coupling and its characteristics," *IEEJ J. Ind. Appl.,* vol. 11, no. 1, pp. 76−87, Jan. 2022.

[12] B. J. Ebot and Y. Fuiimoto, "A general framework for the analysis and design of a wireless resonant motor," in *Proc. IEEE Int. Elect. Mach. Drives Conf.*, May 2019, pp. 1966−1970.

[13] B. J. Ebot and Y. Fujimoto, "A motor design based on wireless magnetic resonance coupling technology," in *Proc. IEEE Energy Convers. Congre. Expo.,* Oct. 2020, pp. 1140−1144.

[14] Z. Jin, M. F. Iacchetti, A. C. Smith, R. P. Deodhar, Y. Komi, A. A. Abdualah, and C. Umemura "A Fast 3-D Winding Inductance Estimation Method for Air-Cored Resonant Induction Machines," in *IEEE Trans. Ind. Appl.,* vol. 58, no. 5, pp. 6125−6135, Sept.−Oct.. 2022.

[15] Z. Jin, M. F. Iacchetti, A. C. Smith, R. P. Deodhar, Y. Komi, A. A. Abdualah, and C. Umemura "Air-Cored resonant induction machines: comparison of capacitor tuning criteria and experimental Validation," in *IEEE Trans. Ind. Appl.,* vol. 57, no. 4, pp. 3595−3606, July−Aug. 2021.

[16] M. F. Iacchetti, R. P. Deodhar, A. C. Smith and K. Mishima "Modelling and operating characteristics of air-cored resonant induction machines," in *Proc. IEEE Energy Convers. Congre. Expo.,* Sept. 2018, pp. 6468−6475.

[17] M. Liu, K. W. Chan, J. Hu, Q. Lin, J. Liu and W. Xu, "Design and realization of a coreless and magnetless electric motor using magnetic resonant coupling technology," *IEEE Trans. Energy Convers.,* vol. 34, no. 3, pp. 1200−1212, Sept. 2019.

[18] M. Vandeputte, L. Dupré and G. Crevecoeur, "Quasi-static torque profile expressions for magnetic resonance-based remote actuation," *IEEE Trans. Energy Convers.,* vol. 34, no. 3, pp. 1255−1263, Sept. 2019.

[19] K. Takishima and K. Sakai, "Analytical and Experimental Investigation of the Frequency Characteristics of an Ultra-Lightweight Motor Based on Magnetic-Resonance Coupling," *2018 XIII Int. Conf. on Elect. Mach (ICEM),* 2018, pp. 562−568.

[20] M. Fu, Z. Tang and C. Ma, "Analysis and optimized design of compensation capacitors for a megahertz WPT system using full-bridge rectifier," *IEEE Trans. Ind. Informat.,* vol. 15, no. 1, pp. 95−104, Jan. 2019.

[21] Z. Jin, M. F. Iacchetti, A. C. Smith, R. P. Deodhar and K. Mishima, "Comparison of different capacitor tuning criteria in air-cored resonant induction machines," in *Proc. IEEE Energy Convers. Congre. Expo.,* Sept. 2019, pp. 3017−3024.

[22] F. Barrero and M. J. Duran, "Recent Advances in the Design, Modeling, and Control of Multiphase Machines − Part I," *IEEE Trans. Ind. Electron.,* vol. 63, no. 1, pp. 449−458, Jan. 2016.

[23] J. -G. Kim, G. Wei, M. -H. Kim, J. -Y. Jong and C. Zhu, "A Comprehensive Study on Composite Resonant Circuit-Based Wireless Power Transfer Systems, " *IEEE Trans. on Ind. Electron.*, vol. 65, no. 6, pp. 4670-4680, June 2018.

[24] L. Zhu, L. Wang, M. Wu, C. Zhao and L. Yu, "Precise Modeling and Design of Self-Resonant for High-Efficiency Mid-Range Wireless Power Transfer System," *IEEE Trans. Power Electron.*, vol. 38, no. 6, pp. 7848-7862, June 2023.

Besong John Ebot (Member, IEEE) received the M.E., and Ph.D., degrees in electrical and computer engineering from Yokohama National University, Yokohama, Japan, in 2018, and 2023 respectively.

Since 2023, he has been with the Typhoon Science and Technology Research Center at the Institute for Multidisciplinary Sciences of Yokohama National University as a Visiting Researcher. His research interests are in electric machine design and drives.

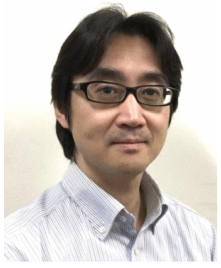

Yasutaka Fujimoto (Senior Member, IEEE) received the B.E., M.E., and Ph.D. degrees in electrical and computer engineering from Yokohama National University, Yokohama, Japan, in 1993, 1995, and 1998, respectively, where he is currently a Professor. His research interests include actuators, robotics, manufacturing automation, and motion control.

Dr. Fujimoto is a Senior Member of IEE of Japan and a member of Robotics Society of Japan. He was the recipient of the IEEE/ASME Transactions on Mechatronics Best Paper Award in 2020. He is an Associate Editor for IEEE TRANSACTIONS ON INDUSTRIAL ELECTRONICS and a Vice Chief for the *IEEJ Journal of Industry Applications.*